

Vessel Tractography Using an Intensity based Tensor Model with Branch Detection

Suheyla Cetin*, Ali Demir, Anthony Yezzi, Muzaffer Degertekin, and Gozde Unal*

Abstract—In this paper, we present a tubular structure segmentation method that utilizes a second order tensor constructed from directional intensity measurements, which is inspired from diffusion tensor image (DTI) modeling. The constructed anisotropic tensor which is fit inside a vessel drives the segmentation analogously to a tractography approach in DTI. Our model is initialized at a single seed point and is capable of capturing whole vessel trees by an automatic branch detection algorithm developed in the same framework. The centerline of the vessel as well as its thickness is extracted. Performance results within the Rotterdam Coronary Artery Algorithm Evaluation framework are provided for comparison with existing techniques. 96.4% average overlap with ground truth delineated by experts is obtained in addition to other measures reported in the paper. Moreover, we demonstrate further quantitative results over synthetic vascular datasets, and we provide quantitative experiments for branch detection on patient Computed Tomography Angiography (CTA) volumes, as well as qualitative evaluations on the same CTA datasets, from visual scores by a cardiologist expert.

Index Terms—segmentation, tubular structures, branch detection, vessel trees, coronary arteries, tensor estimation, tractography, Computed Tomography Angiography (CTA)

I. INTRODUCTION

SEGMENTATION of coronary arteries is a fundamental step for accurate visualization of vessels and assessment of cardiovascular diseases. Computationally created 3-Dimensional (3D) models of arteries are used as a virtual medical navigation tool and in investigation of possible anomalies in arteries. Coronary artery segmentation attempts at either directly a vessel-lumen surface extraction, or central lumen line and diameter estimation in different medical image modalities, particularly, Computed Tomography Angiography (CTA). Segmentation of coronary arteries is a challenging task. This is typically due to the small size of the vessels compared to the image resolution, the presence of (motion) artifacts in the data, the presence of neighbouring structures with similar intensities as the vessel, and pathologies such as severe stenoses and calcifications.

In the past decade, various sophisticated vascular segmentation algorithms have been developed, and several reviews

Suheyla Cetin, Ali Demir, and Gozde Unal are with the Faculty of Engineering and Natural Sciences, Sabanci University, Istanbul, Turkey, 34956; E-mails: suheylacetin@sabanciuniv.edu, gozdeunal@sabanciuniv.edu. Asterisks(*) indicate the corresponding authors.

Anthony Yezzi is with the School of Electrical Engineering, Georgia Institute of Technology, Atlanta, GA, USA.

Muzaffer Degertekin is with the Department of Cardiology, Yeditepe University Hospital, Istanbul, Turkey, 34752.

Copyright (c) 2012 IEEE. Personal use of this material is permitted. However, permission to use this material for any other purposes must be obtained from the IEEE by sending a request to pubs-permissions@ieee.org.

have been published on vasculature segmentation in the literature [1]–[7]. Vessel segmentation methods can be roughly categorized into three: filtering-based techniques, model-based techniques, and minimal-path techniques.

Earlier vessel segmentation algorithms used filters for vessel enhancement before segmentation. Most well-known filtering techniques are Hessian-based ([8]–[13]), non-linear diffusion ([14]–[16]), and flux-based filtering ([17], [18]). Similarly, other filtering methods for vessel segmentation are based on morphological operators, which analyze images or objects by their interaction with shapes. In particular, mathematical morphology operators that have been involved in vessel segmentation methods include: watershed transform [19], [20], grey-level hit-or-miss transform [21], [22], or connected filtering based on component-trees [23], [24]. The advantage of morphology based vessel segmentation algorithms is that they are mostly automatic. However, structures around the vessel can be detected as vessel and they do not perform well in cluttered/noisy images.

In the second category of vessel segmentation, model-based approaches, explicit vessel models are applied to extract the vasculature. Two main model-based approaches are: (i) deformable models, particularly level-set representations [25]–[27], and (ii) tubular/cylinder models [28], [29]. The level set methods have the advantage of representing surfaces implicitly, hence do not suffer from a re-parameterization problem and provide effortless topology changes of structures. Therefore, the level sets are found useful in segmenting inhomogeneous vascular objects such as blood vessels. However, these advantages also lead to unwanted leakage to surrounding regions when geometrical constraints are not used in the level set function evolution. To address this problem, Nain et al. [30] presented a level-set model with a soft shape prior, which combined image statistics and tubular shape information to segment tubular structures while penalizing leakage. On the other hand, in the tubular/cylinder model category, Friman et al. [29] proposed a tubular tracking algorithm based on a 3D template matching, called Multiple Hypothesis Tracking (MHT), which was used to traverse difficult vessel passages such as those caused by pathologies and areas of low contrast. The algorithm starts from an initial point given on the centerline, and a search tree is built by recursively evaluating possible vessel continuations. Sometimes MHT can terminate earlier; in this case, a minimal path algorithm based on Fast Marching is needed to fill the gaps between newly initialized points and terminated points. The vessel template model presented in [29] had a flatter vessel profile than the Gaussian profile used in [31] and provided flexible central

position, radius and orientation adjustment. Worz et al. [28] proposed tubular vessel models of varying sizes and used a Gaussian-smoothed 3D cylinder, since the 2D cross-sections of medium and large sized vessels were plateau-like and could not be accurately represented by a 2D Gaussian profile.

Minimal path techniques are commonly employed in interactive frameworks, requiring the start and end points for each vessel. Some works have proposed the definition of termination criteria to automatically stop the path propagation and relax the need for end points. For instance, Gulsun and Tek [32] proposed such criteria through heuristic thresholds.

Li and Yezzi [33] proposed a new variant of the traditional, purely spatial minimal path technique by incorporating an additional non-spatial dimension into the search space. They modeled the vessel as a 4D curve, which consisted of three spatial coordinates and an extra non-spatial dimension, which described the thickness at the corresponding 3D point. Thus, each 4D point represented a sphere in 3D space, and the vessel was obtained as the envelope of the family of spheres traversed along this 4D curve. However, Li and Yezzi's model [33] utilized isotropic potentials, and the vessel orientation was not taken into account. To improve this method, Mohan et al. [34] suggested a 4D curves minimal path algorithm which added the radius dimension in a 2D planar disk at each centerline coordinate. Furthermore, they associated to the path an anisotropic potential related to the Finsler metric, which was used in a geodesic active contour approach to estimate the minimal path over the centerline of the vessel as well as the radius. Benmansour and Cohen [35] proposed an interactive vessel segmentation method, which was in the framework of the 4D curves approach of Li and Yezzi [33]. They took into account the vessel orientation by considering an anisotropic metric, which was based on the Optimally Oriented Flux (OOF), introduced by Law and Chung [17]. The designed metric was oriented along the direction of the vessel, admitted higher velocity on the centerline, and provided an estimate of the vessel radius. Lesage et al. [36] created a graph-based method that jointly optimizes the vascular centerline and associated radius on a 4D space-scale graph. It relies on a recursive Bayesian model, and is optimized by minimal path-like techniques, also, it provides a workflow flexibility.

Fully automatic vessel extraction algorithms such as [37], [38] implicitly deal with branching. Interactive methods mostly do not handle branching, since user interaction is provided for every branch. Some semi-automatic methods explicitly represent bifurcations [39] or others perform vascular tree connection after finding the branches [34]. Zhou et al. [40] proposed a learning based method with specially designed filters on cross-sectional planes to automatically detect the bifurcation points of the vessels. Li et al. [41] proposed to use a 4D interactive key point searching scheme. After the key points are located, iteratively, the branches are identified by finding structures between all adjacent key point pairs.

In this paper, following the approaches of introducing orientation information into tubular structure segmentation, we view the vessel segmentation problem from a tensor estimation and tractography perspective as in Diffusion Tensor Imaging (DTI). Our original idea involves estimation of a tensor from

multiple intensity measurements that are constructed by a cylindrical model added on top of the 4D curves model of Li and Yezzi [33]. This cylindrical component introduces directionality into the model, and thus facilitates a tensor fit to the tubular structure (Section II-B). The estimated anisotropic tensor inside the vessel drives the segmentation analogously to a tractography approach in DTI analysis starting from a seed point used as initialization (Section II-C). In addition, we developed a branch detection and unsupervised branch clustering method, which can automatically locate multiple branchings in complex tree structures (Section II-D). Therefore, starting from a seed point, an entire vessel tree can be captured by our technique, which provides the vessel orientation, its centerline (central lumen line) and its thickness (vessel lumen diameter). In this paper, our main application of the developed technique is to 3D modeling of coronary arteries from Computed Tomography Angiography (CTA) scans¹.

We discuss the relation of our method to closely related earlier work. Approaches that are based on the Hessian-based vesselness measures of e.g. Frangi et al. [11] depend on filtering (enhancement) of the whole intensity data, and one drawback as stated by Benmansour et al. [35], is that they include adjacent features, e.g. heart chambers or other organs, as vessels. Benmansour et al. [35]'s method is based on the OOF descriptor, (Law and Chung [17]), which estimates the vessel direction through minimization of a measure of the image gradient, and is only localized around the vessel boundaries. This is a boundary-based approach, whereas the proposed approach is region-based, therefore naturally is more robust to noise in computations. The vessel direction is found as the direction along which the integration of the image gradient sampled on the surface of a sphere is minimal. Benmansour et al. then designed a 4D metric which was partitioned into a 3D symmetric positive definite component and a scalar radius potential. The 3D component of the metric was obtained from the eigenvectors and eigenvalues of the OOF descriptor. Then, the obtained 4D tensor is used in an Eikonal equation as its metric in estimation of the minimal path along the vessel. This is different from our approach, which provides a region-based directional tensor estimation, which samples its measurements from the differences between a cylinder and an inside sphere. Furthermore, as the Benmansour et al. [35]'s method does not provide any branch detection methodology, its level of interactivity is high. Specifically, the following two ideas in adoption of the DTI fiber tracking concept are novel in the vessel segmentation: (i) given a scalar valued 3D volume: construction of the multi-directional regional spatial information over sampling from various directions on the unit sphere \mathbb{S}^2 , and estimation of a rank 2 tensor from the created data; (ii) utilizing the created tensor field in a tractography framework. This is also different from the idea of [34], which utilizes a geodesic active contour framework for surface segmentation. It applies the surface update equations in a Sobolev Space to estimation of white matter bundles, such as the cingulum as one application, whereas in contrast our method applies the well known tractography idea from fiber tracking to the vessel

¹A preliminary version of this work has appeared in [42].

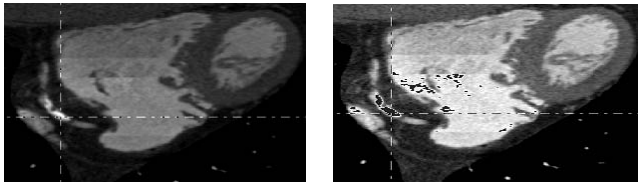
surface segmentation. Mohan et al [34] does not create a rank 2 tensor using the directional cylinders as presented in this paper. Rather, they utilize 2D disks directed along the vessel centerline, and the intensity measurements are taken between the inner disk and the outer annular region. Furthermore, active contour approaches are known to be sensitive to initialization, whereas our streamline tractography approach has a simple correction step for robustness to the initialization and tracking.

II. METHODS

In this section, the details of our tubular structure segmentation method, which we call vessel tractography, are described.

A. Image Preprocessing

Vessel calcifications are not part of the vessel's lumen, for this reason, they are eliminated before applying the vessel tractography algorithm. The images are preprocessed before segmentation to obtain a calcification map first, and later setting the voxel intensity for vessel calcifications equal to the intensity of the myocardial tissue. The basic idea of our method shows similarity to Agatston scoring [43]. However, in our technique, simple statistical analyses of the calcified areas are calculated. In the first step, the cardiologist expert annotates the area of calcifications only on a set of clinical CTA data used for training. After the first and second order statistics on the region of the calcifications are computed, a fixed threshold is obtained and applied automatically on all CTA volumes (further details are in Section III Experimental Results). The obtained calcification map (e.g. see Figure 1) is then used to exclude those intensities in vessel extraction.



(a) An original CT image slice (b) After excluding the calcifications

Fig. 1. An example of the preprocessing step.

B. Intensity Based Tensor Fitting

We develop an intensity based tensor model, which is well-suited to tubular structures as vessels. Although similar to Li and Yezzi's idea [33], a 4D curve representation is used, our novel contributions are three-fold: (1) to bring an anisotropy metric to the measurements model by involving regional measurements from intensity at various spatial directions and using them in a linear least squares tensor fitting to estimate a rank 2 tensor; (2) to adapt brain white matter tractography ideas to vessel tractography, for the first time to our knowledge; (3) to design a new tubular bifurcation detection algorithm.

Our vessel model is constructed as follows:

$$\hat{C}(u) = (c(u), r(u)) \quad , \quad \hat{C} \in \mathbb{R}^4 \quad , \quad u \in [0, L] \quad (1)$$

where $c(u)$ represents the location on a vessel centerline in \mathbb{R}^3 , $r(u) \in [r_{min}, r_{max}] \in \mathbb{R}^+$ represents the radius of a

sphere centered at $c(u)$, and L is the length of the vessel. A sphere at a centerline coordinate point $\mathbf{x}_s \in \mathbb{R}^3$ is denoted by: $sph = (\mathbf{x}_s, r)$. A cylinder along each sampled orientation \mathbf{v} is represented by a stack of disks and denoted as follows:

$$cyl = \bigcup_{l=0, \dots, h} disk(\mathbf{x}_l, r, \mathbf{v}), \quad \mathbf{x}_l = \mathbf{x}_s + \mathbf{v}l, \quad (2)$$

where \mathbf{x}_l is defined as a point in \mathbb{R}^3 , \mathbf{v} is an orientation vector in \mathbb{S}^2 , which also indicates the normal vector to the disk: $disk(\mathbf{x}_l, r, \mathbf{v})$ with radius r , and h is defined as the height of the cylinder (see Figure 2). Next, sampling a set of orientation vectors \mathbf{g}_i over the unit sphere \mathbb{S}^2 , each intensity measurement M_i at the given direction \mathbf{g}_i is an image based feature, which is modeled according to the intensity properties of the vessel. Here, a piecewise constant intensity model is utilized, and the measurement is based on a difference between the intensity mean μ_{Ω_1} of the sphere Ω_1 and intensity mean μ_{Ω_2} of the region Ω_2 , where $\Omega_1 = sph$ and $\Omega_2 = cyl - sph$. These intensity measurements are computed along each orientation vector $\mathbf{g}_i \in \mathbb{S}^2$. Image intensity is denoted by a gray-valued $I : \Omega \in \mathbb{R}^3 \rightarrow \mathbb{R}$ where Ω is the image domain.

Formally, the measurement M_i is expressed as follows:

$$M_i = (\mu_{\Omega_1} - \mu_{\Omega_2})^2, \quad (3)$$

and measurement orientations are defined as a matrix:

$$\mathbf{G} = [\mathbf{g}_1 \quad \mathbf{g}_2 \quad \dots \quad \mathbf{g}_m], \quad (4)$$

where $\mathbf{g}_i = [g_{ix} \ g_{iy} \ g_{iz}]^T$ is the column vector for each measurement orientation and m is the number of orientations represented on \mathbb{S}^2 . For now, let \mathbf{g}_v represent the vessel direction vector. For \mathbf{g}_i s.t $\mathbf{g}_i^T \mathbf{g}_v = 0$, M_i becomes large, as the intensity distribution changes less along the vessel direction, and more along the orthogonal directions. Moreover, M_i becomes maximum when Ω_1 fits to the vessel, and Ω_2 is outside the vessel.

Using a 3×3 tensor, which is a symmetric positive definite matrix:

$$\mathbf{D} = \begin{bmatrix} d_{11} & d_{12} & d_{13} \\ d_{12} & d_{22} & d_{23} \\ d_{13} & d_{23} & d_{33} \end{bmatrix}, \quad (5)$$

M_i can be modelled as:

$$M_i = \mathbf{g}_i^T \mathbf{D} \mathbf{g}_i. \quad (6)$$

In general, a matrix $\mathbf{D} \in \mathbb{R}^{n \times n}$ is said to be positive semi-definite if $\mathbf{x}^T \mathbf{D} \mathbf{x} \geq 0$, for all $\mathbf{x} \neq \mathbf{0}$ in \mathbb{R}^n . The tensor \mathbf{D} is expected to be symmetric positive semi-definite as the measurements M_i are non-negative, however, due to noise in the data, one is usually not guaranteed to recover all \mathbf{D} 's with this property unless one includes it explicitly as a constraint.

After the measurements $M_{m \times 1}$ are calculated for all orientations, to solve for the tensor \mathbf{D} from $M_i = \mathbf{g}_i^T \mathbf{D} \mathbf{g}_i$, $i = 1, \dots, m$ equations, we utilize a least squares fitting. We stack the six components of \mathbf{D} into a vector, since \mathbf{D} is a symmetric matrix, as:

$$\mathbf{d} = [d_{11} \quad d_{22} \quad d_{33} \quad d_{12} \quad d_{13} \quad d_{23}]^T \quad (7)$$

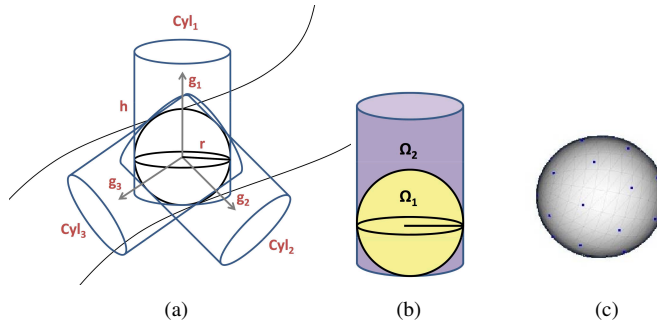


Fig. 2. Illustrations of (a) directional measurement model: each Cyl_i is characterized by the direction vector \mathbf{g}_i , the height h , and the disk centered at point \mathbf{x}_i with radius r ; (b) cylinder and sphere regions for intensity measurements; (c) orientations on unit sphere* (sphere picture in (c) is from BioImage Suite Tool, Yale University School of Medicine).

and re-arrange Eq. (6) to get

$$M_i = \mathbf{H}_i \mathbf{d}, \quad (8)$$

where \mathbf{H}_i is the i^{th} row of the matrix, which is constructed as follows:

$$\mathbf{H} = \begin{bmatrix} g_{1x}^2 & g_{1y}^2 & g_{1z}^2 & 2g_{1x}g_{1y} & 2g_{1x}g_{1z} & 2g_{1y}g_{1z} \\ \vdots & \vdots & \vdots & \vdots & \vdots & \vdots \\ g_{mx}^2 & g_{my}^2 & g_{mz}^2 & 2g_{mx}g_{my} & 2g_{mx}g_{mz} & 2g_{my}g_{mz} \end{bmatrix} \quad (9)$$

In matrix form, Eq. 8 becomes $\mathbf{M} = \mathbf{H}\mathbf{d}$. Linear least squares fitting is applied to solve for \mathbf{d} :

$$\mathbf{d} = (\mathbf{H}^T \mathbf{H})^{-1} \mathbf{H}^T \mathbf{M}. \quad (10)$$

Once \mathbf{d} is obtained, we construct the vessel tensor \mathbf{D} , simply as in Eq. (5). The least squares method also utilized in DTI literature (e.g. [44]) generally gives good results for noisy datasets, since more measurements than needed (usually $m \gg 7$) are used in the estimation process. However, it is possible to occasionally obtain negative tensors (i.e tensors with negative eigenvalues). After the tensor estimation, one needs to check the tensor positivity, and re-project the negative tensors onto the positive tensors space. This is generally done by forcing the negative eigenvalues of the tensor to zero:

$$\tilde{\mathbf{D}}(x, y, z) = \tilde{\lambda}_1 \mathbf{u}_1 \mathbf{u}_1^T + \tilde{\lambda}_2 \mathbf{u}_2 \mathbf{u}_2^T + \tilde{\lambda}_3 \mathbf{u}_3 \mathbf{u}_3^T, \quad (11)$$

$\forall (x, y, z) \in \Omega$ where $\lambda_1, \lambda_2, \lambda_3$ are the eigenvalues and $\mathbf{u}_1, \mathbf{u}_2, \mathbf{u}_3$ are the eigenvectors of \mathbf{D} with $\tilde{\lambda}_i = \max(0, \lambda_i)$. Note that this projection minimizes the Frobenius norm between \mathbf{D} and $\tilde{\mathbf{D}}$. Since the eigenvalue of the principal direction is always positive (unless all eigenvalues are negative which should not be encountered), \mathbf{u}_1 , the principal vector of the tensor does not change after the projection in DTI modeling. In our vessel tensor model, the estimated tensor will be forced to positive definiteness via an absolute value operation, which will be discussed next after the final tensor estimation.

1) *Vessel Lumen Thickness Estimation*: As explained above in subsection II-B, the tensor estimation depends on the radius parameter of the measurements model. Furthermore, the thickness of the vessel lumen is directly related to the radius of the model, as the lumen radius is to be obtained when there is a perfect fit of the model to the data. Therefore, the tensors

are first estimated for multiple radii, and the tensor with the “best radius” is selected as explained next.

To estimate the final tensor \mathbf{D} , which describes the direction of the vessel and the radius of the sphere, the tensor \mathbf{D}^r is calculated $\forall r \in [r_{min}, r_{max}]$ at a point inside the vessel. When the diameter of the sphere is below or above the true vessel lumen thickness, the measurement M_i^r becomes lower. The M_i^r thus becomes the largest with the sphere which is tangent to the vessel and, hence the radius of the sphere is detected as:

$$\hat{r} = \underset{r}{\operatorname{argmax}} \|\mathbf{D}^r\|, \forall r \in [r_{min}, r_{max}], \quad (12)$$

where $\|\cdot\|$ denotes the 2-norm of the matrix \mathbf{D}^r . That is, the norm of the tensor in Eq. (12) happens to be the largest when the sphere fits to the vessel boundary. After the tensor \mathbf{D}^r is computed, it is decomposed into its eigenvalues and eigenvectors using SVD (Singular Value Decomposition): $\mathbf{D}^r = \mathbf{V}_r \boldsymbol{\lambda}_r \mathbf{V}_r^T$, where $\boldsymbol{\lambda}_r = \operatorname{diag}\{\lambda_1^r, \lambda_2^r, \lambda_3^r\}$ is the diagonal matrix with the eigenvalues, and $\mathbf{V}_r = [\mathbf{v}_1^r, \mathbf{v}_2^r, \mathbf{v}_3^r]$ are the eigenvectors of the tensor.

As the measurement, M_i , is the lowest along the vessel direction and larger along the orthogonal directions, the tensor \mathbf{D} consists of two major eigenvectors, so it becomes a planar ellipsoid ($\lambda_1 \approx \lambda_2 \gg \lambda_3$). Shape of the tensors on the centerline are more planar and have bigger norm than the tensors nearer to edges. In addition, when the radius of the sphere-cylinder model is smaller or larger than the true radius of the vessel, the norm of the tensor becomes lower.

The 2-norm of symmetric matrices corresponds to the largest λ , here λ_1^r , of the \mathbf{D}^r . For an expected planar tensor, there are two large eigenvalues that can be utilized, then the Eq. (12) can be alternatively expressed as follows:

$$\hat{r} = \underset{r}{\operatorname{argmax}} |\lambda_1^r + \lambda_2^r|, \forall r \in [r_{min}, r_{max}]. \quad (13)$$

This idea has resemblance to the scale-space approaches where the calculations are done over multiple scales, and an optimal scale in terms of typically the standard deviation parameter of a Gaussian kernel is selected at each volume coordinate (e.g. as in Frangi’s method [11]). Estimated tensor \mathbf{D} is now equal to $\mathbf{D}^{\hat{r}}$. As a result, \mathbf{v}_3 is the eigenvector corresponding to the smallest eigenvalue of the tensor, and it represents the vessel orientation. By SVD decomposition,

the eigenvalues of the tensor are forced to be non-negative [45]. Particularly, for the symmetric square matrix \mathbf{D} , its singular values are the absolute values of its eigenvalues. This enforcement of positivity works to our advantage, as in our tensor model, the vessel orientation is determined by \mathbf{v}_3 , and problematic negative eigenvalues are either mapped to a large positive number or if they were small in magnitude, they would still retain their small magnitude after $|\cdot|$ operation. Therefore, SVD provides a desired positive-definite tensor solution. As the tensor's norm is preserved, and it is not reconstructed after the tensor projection, this does not constitute a problem.

To illustrate estimated tensors, a synthetic Y-shaped vessel volume [46] at a constant thickness is utilized, which is shown in Figure 3(a). Norm of the tensor is plotted as a function of sphere radius in Figure 3(b). For instance, the norm at radius 3 becomes maximum for a specific voxel chosen from the centerline of the synthetic vessel. In Figure 4, the tensors for the Y-shaped vessels are depicted for radii 2, 3 and 4 respectively. As can be observed, the norm of the tensors on the centerline for the true radius are the largest compared to those of all other radius estimates.

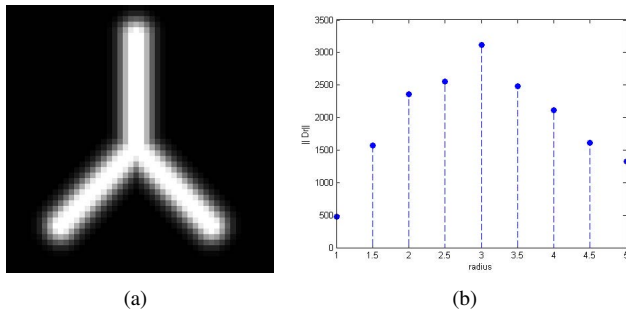


Fig. 3. Example of vessel lumen thickness estimation: (a) $60 \times 60 \times 60$ synthetic vessel volume with a constant radius of 3; (b) Norm of the tensor \mathbf{D}^r for a voxel on the centerline of the synthetic data, for a range of radius r .

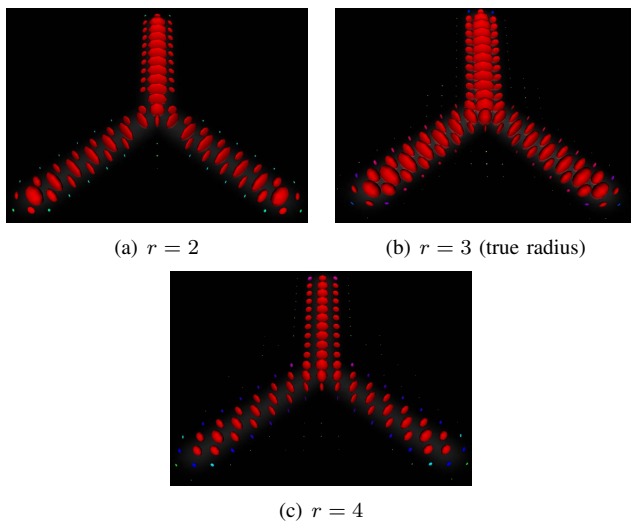


Fig. 4. Estimated tensors using radii 2, 3, and 4 for $60 \times 60 \times 60$ synthetic vessel volume.

C. Vessel tractography

We define a vessel tractography, which traces the centerline of a vessel using the intensity based tensor \mathbf{D} , inspired by the DTI tractography that uses a diffusion tensor. Vessel tractography starts with a user defined initial seed point. The seed point is preferably selected at the center of one of the cross sections of the vessel. The tract, i.e. the 3D centerline, starts to propagate along the positive and negative directions of the eigenvector corresponding to the smallest eigenvalue of the planar tensor. For all spatial coordinates along the tract, the tensor is calculated as explained in Section II-B. The minor eigenvector of the tensor, \mathbf{v}_3 is obtained at the current coordinate $\mathbf{c}(u_{n-1})$, and a new tract coordinate $\mathbf{c}(u_n)$ is calculated by adding the \mathbf{v}_3 to $\mathbf{c}(u_{n-1})$. This is in fact the streamline tractography (SLT) approach [47] in DTI, which uses the vessel orientation by weighting it with α to compute an Euler's method approximation to the parametrized tract $\mathbf{c}(u)$ as follows:

$$\mathbf{c}(u_n) = \mathbf{c}(u_{n-1}) + \alpha \frac{d\mathbf{c}(u)}{du} \rightarrow \mathbf{c}(u_n) \approx \mathbf{c}(u_{n-1}) + \alpha \mathbf{v}_3, \quad (14)$$

where $\mathbf{c}(u=0)$ is the seed point, and $0 \leq u_n \leq L$, L is the length of the vessel. The tract is computed by taking a piecewise linear step ($0 \leq \alpha \leq 1$) in the direction of \mathbf{v}_3 , hence tract propagation occurs in vessel tangential direction approximated by \mathbf{v}_3 (See Figure 5).

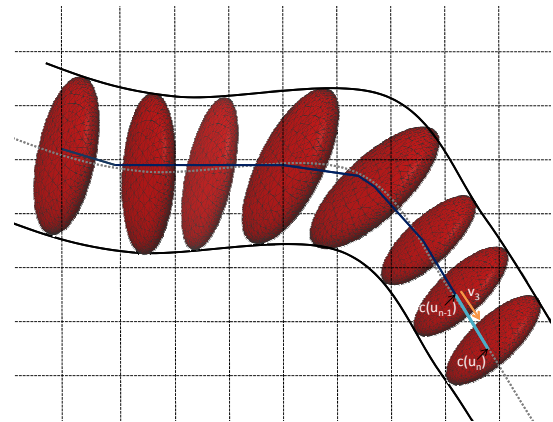


Fig. 5. Illustration of the vessel tractography: Centerline of the vessel (black) is shown by gray. Extracted vessel tract until the current coordinate $\mathbf{c}(u_{n-1})$ is depicted by (navy blue). On the distal part of the tract (turquoise); minor vector of the planar tensor, \mathbf{v}_3 , current location, $\mathbf{c}(u_{n-1})$, and how the tract is obtained by adding the \mathbf{v}_3 direction to the current location $\mathbf{c}(u_{n-1})$ are shown.

The tractography algorithm continues till pre-defined convergence criteria are satisfied:

- First convergence criterion is the mean intensity ratio between the spherical region of the seed and that of the current coordinate $\mathbf{c}(u_{n-1})$. The sphere centered at the seed point is defined as $sph_0 = (\mathbf{c}_{seed}, r_{seed})$ and sphere at the current coordinate $\mathbf{c}(u_{n-1})$ is $sph_1 = (\mathbf{c}(u_{n-1}), r)$, and the regions are specified as $\Omega_0 = sph_0$ and $\Omega_1 = sph_1$. If the ratio $\mu_{\Omega_1}/\mu_{\Omega_0}$ is below a given threshold (β_0), this implies that the tract reaches the end

of the vessel and the tractography stops at this point (See Figure 6(a)).

- Second termination criterion is defined from the ratio $\beta_1 = \mu_{\Omega_3} / \mu_{\Omega_1}$, where $\Omega_3 = sph_3 - sph_1$ and $sph_3 = (c(u_{n-1}), 2r)$ (See Figure 6(b), 6(c)). When $c(u_{n-1})$ reaches the origin (e.g. coronary ostium) or the end of artery, β_1 is assumed to be approximately 1. β_1 is used both to force tract to stop at the end of vessel and to prevent the tract from diverging towards regions around the vessel.
- Third criterion, which stops the tract when the radius r at point $c(u_{n-1})$ reaches to $r = r_{max}$, is used to avoid divergence of the vessel tract to surrounding blob regions.

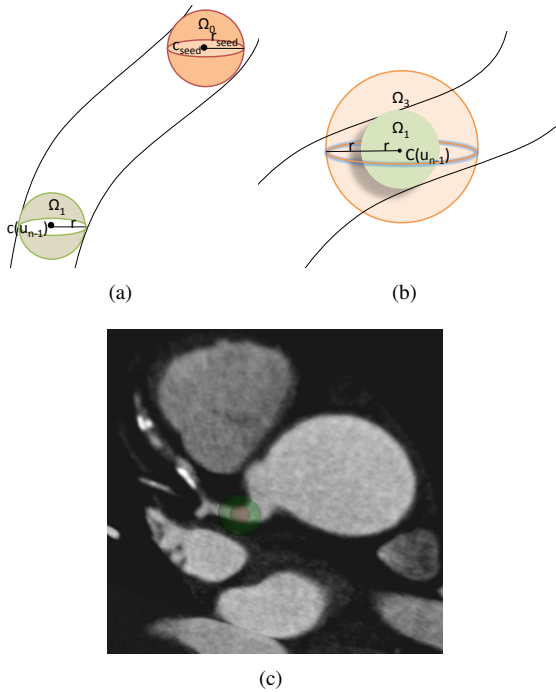


Fig. 6. Illustration of the regions (spheres): (a) Ω_0 and Ω_1 ; (b) Ω_1 and Ω_3 ; (c) An example of the Ω_1 (red) and Ω_3 (green) are shown on a CTA volume.

Centralization: A tract or a centerline of the vessel sometimes can aberrate because of tensor perturbation due to numerical errors in its modeling and estimation, imaging process, and such effects. In this case, a centralization procedure should be applied to the tract. First, a multiplanar reconstruction method (MPR) is applied at the coordinate $c(u_{n-1})$ to find a projection slice which has v_3 as its normal vector. Then, v_1 and v_2 define the reconstructed plane. A single MPR plane image around the current coordinate is defined as

$$I_{prj}(i, j) = I(c(u_{n-1}) + (i - x_c)v_1 + (j - y_c)v_2), \quad (15)$$

where I is the original image to be projected, I_{prj} is the projection image and x_c, y_c are the coordinate centers of the I_{prj} . After the subregion or projected plane around the coordinate through v_1 and v_2 is calculated, then an $r \times r$ (r is the radius found during tensor fitting) kernel is applied on this plane to find the coordinate, which is the center of a maximum brightness region.

This plane is chosen to be large enough to involve the vessel boundaries and surroundings near the vessel, but not very large to compromise other structures around the vessel. Let (x', y') represent the coordinates of the maximum brightness point, which is found in following way:

$$(x', y') = \operatorname{argmax}_{x, y} \sum_{i, j \in N(x, y)} I_{prj}(i, j), \quad (16)$$

where the neighbourhood function $N(x, y)$ is expressed as:

$$N(x, y) = \{(i, j) | (x - i)^2 + (y - j)^2 \leq r^2\}. \quad (17)$$

Then the corresponding point in the original image is defined as

$$c' = c(u_{n-1}) + (x' - x_c) \frac{v_1}{2} + (y' - y_c) \frac{v_2}{2} \quad (18)$$

where c' is the centralized point, which is the corrected centerline coordinate.

D. Branch Detection - Unsupervised Clustering

In order to extend our vessel tractography model to tubular trees, we developed a branch detection method. It is inspired from the Mohan et al. work [34], which was based on an assumption that vessels have at most two branches to be separated. Their algorithm checks the surrounding regions around the center coordinate $c(u_{n-1})$ and cluster them via a K-means clustering, with $K=3$ including the main branch.

We propose an unsupervised clustering method, which is capable of detecting any number of branchings from a parent coordinate. In our method, we assume that the branches of the vessel tree have similar intensity distributions with the main branch. We search the branches on a spherical surface around the current coordinate in a forward field of view (see Fig. 7), which avoids the branch candidates that are already processed. Branch candidate coordinates are calculated as:

$$c(i) = c(u_{n-1}) + 2r\mathbf{g}_i, \quad \mathbf{g}_i \in \mathbf{g} \quad (19)$$

where \mathbf{g} represents orientations on \mathbb{S}^2 as defined in Section II-B.

The intensity mean of the sphere, μ_{sph_1} , centered at the potential branch coordinate, $c(i)$, is defined inside a sphere $sph_1 = sph(c(i), r)$, and the intensity mean of the sphere, μ_{sph_0} , centered at the seed coordinate, c_{seed} is calculated inside $sph_0 = (c_{seed}, r_{seed})$. Intensity mean ratio, β_1 , is applied for the potential branch candidates using $\mu_{sph_1} \geq \mu_{sph_0} \beta_1$. When the potential branch candidate has a mean intensity higher than $\mu_{sph_0} \beta_1$, the tensor fitting is applied at that coordinate, otherwise it is eliminated. Direction of the vectors are used as a cluster feature in our method. If v_3 of the tensor of the potential branch coordinate is not in the direction of the current path, v_3 and its coordinate is put into a new cluster or to an already existing cluster as follows:

- 1) When the vector v_3 is closer to the directions in one of the previously formed clusters, it is inserted into an appropriate cluster with its corresponding coordinate;
- 2) When the vector v_3 has a distinct orientation, a new cluster is constructed, and this vector is added with its corresponding coordinate to that cluster.

Figure 7 depicts the eliminated branch candidates, and branch coordinates that are clustered using our method. Black balls represent the coordinates that are eliminated. On the other hand, red balls represent the coordinates that are clustered. In the Y-shaped vessel, two branches are found and clustered.

To increase the number of samples in each cluster, detected branch coordinates and orientation vectors are stacked into clusters in a $2r$ voxel distance away from the first coordinate that detected the branches. Then, the coordinate mean of each cluster is calculated and labelled as a branch coordinate. The proposed branch detection algorithm is summarized in Algorithm 1. The algorithm is based on the assumption that the vessel displays greater intensity than structures surrounding the vessel that have a size similar to that of a vessel. We perform branch detection step each time the current point $c(u_{n-1})$ moves one unit, i.e. when there is 1 voxel difference between its last location where a branch check was performed.

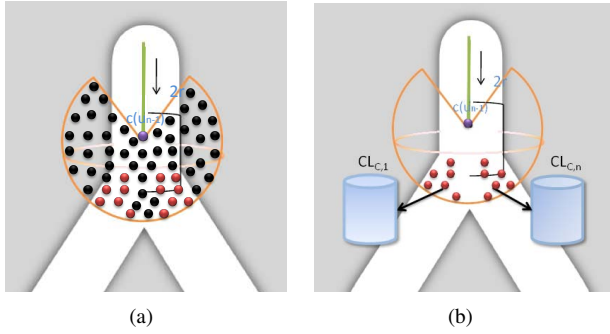


Fig. 7. (a) Branch Elimination process; Black balls: eliminated coordinates, Red balls: coordinates that will be clustered in the next step. (b) Clustering of branch coordinates; Y-shaped vessel splits into two clusters.

The estimated tensors are shown on several sample coronary arterial branches in Figure II-D over real CTA volumes. It can be observed that tensor fitting works reasonably well over challenging vessel regions such as stenotic areas (Case 2); branchings (Case 3), noisy intensity scenarios (Case 4 and 5), and nearby high-contrast regions (Case 5). For the latter case, i.e. with a neighboring cluttering region in a certain direction, a good tensor fit was possible due to sampling of measurements from the majority of the remaining directions. Indeed, for such perturbations, our algorithm involves a centerline correction step as explained in Section II-C.

III. EXPERIMENTAL RESULTS

In this section, we present our validation experiments in four parts: (a) synthetic experiments; (b) Rotterdam Coronary Artery Algorithm Evaluation Framework; (c) qualitative scoring of clinical cases; (d) quantitative validation of branch detection.

We first give a quantitative validation of the performance of the vessel tractography method on synthetic vascular image volumes, which are obtained from the work of Hamarneh and Jassi's [48] that simulate volumetric images of vascular trees and generate the corresponding ground truth segmentations. In these synthetic data experiments, we evaluate the performance of the segmentation and bifurcation detection together. We

Algorithm 1 Branch Detection algorithm - Unsupervised Clustering Method

Input: Sample N directions $g_i, \forall i \in (1, N)$ uniformly off the sphere S^2 , μ_{seed} intensity mean of the sphere centered at c_{seed} with radius r_{seed} , mean threshold β_1 , angle thresholds A_1, A_2 and Cl_C (clusters of branch coordinates), Cl_V (clusters of orientation vectors). The clusters are cleared at the coordinate where the junction is detected for the first time.

Output: Updated Cl_C, Cl_V .

for do $i \in (1, N)$

· Check similarity of directions g_i and v_3 :

$g_i^T v_3 < \cos(A_1)$ to avoid searching the branches in the previously processed voxels.

· Find a branch candidate $c(i)$ using Eq. (19).

· Eliminate the candidate coordinate $c(i)$, if it is labelled as processed (the coordinates already processed are labelled by a spherical mask with the estimated r).

· Apply the tensor fitting as explained in Section II-B; find $r(i)$ (radius), $v(i)$ (vessel direction) and $\mu(i)$ (mean of the sphere with radius $r(i)$ centered at $c(i)$) of the tensor at $c(i)$.

· Eliminate the candidate coordinate $c(i)$ for:

a) v_i that has overlap with the parent vector v_3 ;

b) $r = r_{max}$;

c) $\mu(i) < \mu_{seed} \beta_1$.

if Cl_C or Cl_V is empty **then**

Create a new cluster in Cl_V and insert $v(i)$ into that cluster.

Create a new cluster in Cl_C and insert $c(i)$ into that cluster.

else

for do all vectors in each Cl_V

if v_i has a similar orientation with

$w \in Cl_V: v_i^T w < \cos(A_2)$ **then**

Insert v_i to an appropriate cluster in Cl_V .

Insert c_i to an appropriate cluster in Cl_C .

else

Create a new cluster for v_i and c_i ;

insert them to Cl_V and Cl_C .

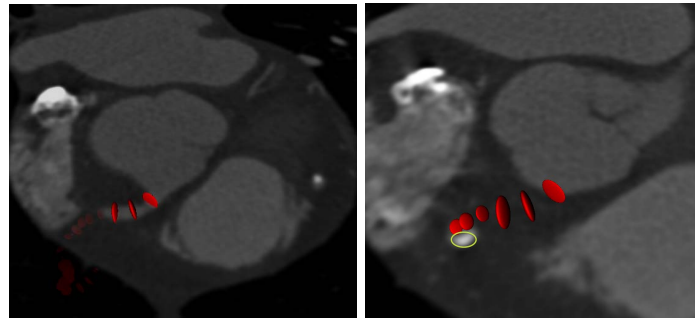
end if

end for

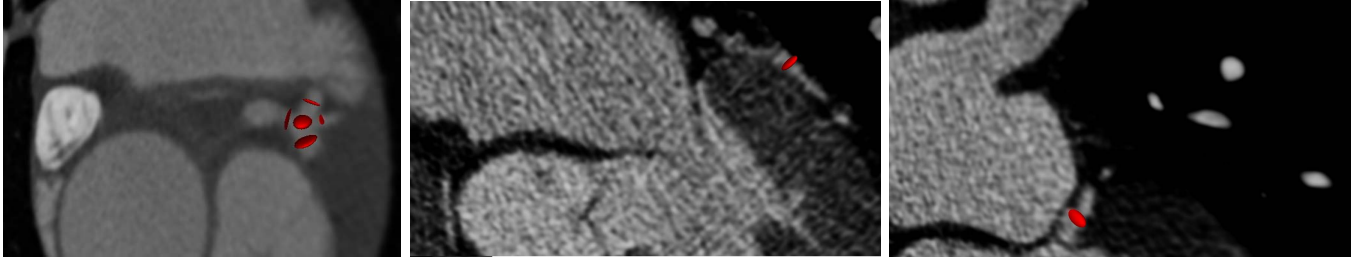
end if

end for

also perform experiments by adding different levels of salt & pepper, and Gaussian noise, and comparing our results by a generic segmentation algorithm. In the second part, we demonstrate the quantitative performance of our method on Rotterdam Coronary Artery Evaluation Framework [49], [50], which facilitates testing over worldwide standard datasets and comparison to existing state-of-the-art algorithms in the literature. They provide 8 training datasets with ground truths and 24 test datasets for performance measures among several methods. Next, we extracted the coronary arteries from patient CTA volumes acquired at our clinical site, and evaluated our



(a) Case 1: Axial slice cuts the proximal region, the norm of the tensors are large in these regions. (b) Case 2: Axial slice cuts the stenotic region (green), the norm of the tensors become smaller in these regions.



(c) Case 3: Tensor fitting example at branch points. (d) Case 4: Tensor fitting example on a CTA volume with noisy intensity acquisition. (e) Case 5: Tensor fitting example on a branch with nearby high-contrast region structure.

Fig. 8. Estimated tensors are depicted (red) on the axial slices of CTA images of Case 1, 2, 3, 4 and 5.

method by qualitative scores of a cardiologist expert. We collected 10 cardiac CTA datasets from Cardiology Department of Yeditepe University Hospital, which were acquired from a Philips Brilliance 64 slice CTA machine. The datasets are contrast enhanced and average voxel size of the datasets is $0.43 \times 0.43 \times 0.45 \text{ mm}^3$. The data set was obtained from a series of patients presenting with stable angina pectoris. Three patients had previous myocardial infarction. For the synthetic and qualitative validation cases, a single seed point is selected from each tree, then the entire vessel tree is segmented automatically.

The parameters of the algorithm are estimated from several experiments:

- Regions of severe and moderate calcifications are quantitatively evaluated on 15 datasets. First, the datasets are brought to the same intensity scale in order to specify the calcium threshold from a more certain intensity range, then the calcified regions are annotated by the cardiologist expert. First and second order intensity statistics are evaluated in these regions, the average maximum and minimum intensities are found in a training set, then all CTA volumes are rescaled. The calcium thresholding parameter is determined on these volumes as 1743 ± 104.41 (mean \pm standard deviation). We selected a typical value, $t_{calc} = 1700$, as a threshold, and applied to the datasets in the preprocessing step of our method.
- In order to estimate the height of the cylinder in our vessel model, the range of height scales 2, 4 and 6 is selected, and applied to the training dataset of the Rotterdam database [51]. Dice overlap ratio (OV=OM, which will be mathematically expressed in the validation step) is

selected as a metric to compare the performances. $h = 4r$ has the highest OV value (See Table I); due to the fact that $h = 2r$ contains minimal background information and $h = 6r$ contains unnecessary background samples, they perform worse than $h = 4r$. Therefore, $h = 4r$ is selected as the height of the cylinder model.

- We perform experiments on the training dataset of the Rotterdam database to estimate the number of directions needed for tensor fitting (See Table II). Minimum value of m is selected as 6, since the tensor has 6 degrees of freedom (DOF). The OV measure for 6, 15, 24, and 32 number of unit directions on \mathbb{S}^2 are calculated, from which $m = 24$ gives the best overlap measure. The OV scores for larger m , (e.g. $m = 32$), do not improve as the measurements taken with larger number of directions start to overlap due to the thickness of the cylinder model.
- To estimate the number of directions on \mathbb{S}^2 for branch detection (N), we tested our method on the three complex structured vascular dataset of Hamarneh and Jassi's [48], in which we selected N as 32, 64, 128 and 256 respectively (See Table III for the performance results). Although the OV value of $N = 256$ is slightly better than $N = 128$, comparing the runtime of our algorithm in both cases led us to select $N = 128$ as a number of unit directions for branch detection.
- $\alpha = 0.15$ which is the step size in SLT.
- The initial radius range is selected between 0.25 and 4 mm in tensor fitting. The coronary artery radius values can be variable from a patient to a patient. Therefore, we selected the minimum and maximum radii range to include all possible anatomical variability due to having

TABLE I
PERFORMANCE FOR DIFFERENT HEIGHT SCALES IN THE CYLINDER
MODEL

Dataset Number	H=2	H=4	H=6
0	0	95.95	78.87
1	2.02	99.55	72.83
2	3.50	98.52	94.10
3	2.81	91.25	98.54
4	1.76	96.25	97.72
5	4.20	99.15	74.04
6	4.27	99.33	99.4
7	3.63	97.1	85.67
Avg. Overlap Ratio	2.77	97.14	85.67

TABLE II
PERFORMANCE FOR DIFFERENT NUMBER OF DIRECTIONS IN TENSOR
FITTING

Dataset Number	M=6	M=15	M=24	M=32
0	44.95	78.71	95.95	96.01
1	82.60	93.59	99.55	99.48
2	41.64	90.12	98.52	96.79
3	61.82	82.39	91.25	90.72
4	57.32	85.27	96.25	96.32
5	70.81	79.90	99.15	97.85
6	59.80	90.58	99.33	97.89
7	67.03	82.45	97.1	88.19
Avg. Overlap Ratio	60.75	85.38	97.14	95.41

several diseases, age, and origin of a patient. This range certainly can be changed according to the anatomical application region.

- Algorithm's termination ratios β_0 and β_1 are chosen as 0.25 and 0.85 at the end of an analysis of the mean intensity regions μ_{Ω_0} , μ_{Ω_1} , and μ_{Ω_3} (Section II-C): From the training dataset of the Rotterdam database, 10 voxels are selected from the proximal and distal regions of each coronary artery, then the average mean intensity regions with the standard deviations are calculated for these regions separately. In Table IV, the mean intensity of regions μ_{Ω_0} , μ_{Ω_1} , and μ_{Ω_3} are shown along with the ratios $\mu_{\Omega_1}/\mu_{\Omega_0}$ and $\mu_{\Omega_3}/\mu_{\Omega_1}$. β_0 is selected as a low end value (0.25) from the range of 0.307 ± 0.063 to guarantee finding of the small vessels. We select β_1 as 0.85 above than average $\mu_{\Omega_3}/\mu_{\Omega_1}$ between $\mu \pm 2\sigma$ and $\mu \pm 3\sigma$, to avoid misleading stoppings. Thus, the small vessels are still guaranteed to be found. In addition, this approach also guarantees that leakage to the regions like aorta.
- Angle parameters used in branch detection A_1 and A_2 are heuristically set through experiments on a small training subset from the Rotterdam training database [51]. They are selected as $\frac{5\pi}{3}$, and $\frac{\pi}{9}$ respectively.
- MPR image plane size (Section II-C), is selected as $10mm \times 10mm$, which anatomically is guaranteed to contain the coronary vessel.

To increase the computational efficiency of our algorithm, the radius range $0.25mm$ and $4mm$ is applied only at the seed coordinate. After finding the initial radius r by tensor fitting,

TABLE III
PERFORMANCE FOR DIFFERENT NUMBER OF DIRECTIONS IN BRANCH
DETECTION

Number of directions	32	64	128	256
Data 1	72.92	89.93	93.03	93.48
Data 2	81.73	90.42	93.76	93.89
Data 3	80.49	91.78	95.70	96.03
Avg. Overlap Ratio	78.38	90.71	94.16	94.47

the radius range is selected between $r - 3$ and $r + 3$, which avoids unnecessary computations of tensor fitting over a large range of radii. Moreover, introduced radius dependency results in a smoother path, as the radius range gets narrower in tensor fitting, and the radius becomes more dependent on the radius of the previous coordinate, hence this acts as a smoothness constraint.

The proposed vessel tractography algorithm is fully implemented in C++ environment, using Qt [52] and VTK [53] libraries for visualization.

A. Synthetic Validation

Ten datasets that simulate volumetric gray-valued images of vascular trees and create the corresponding ground truth segmentations and bifurcation points, are generated for synthetic validation of vessel extraction and branch detection using the VasculSynth Software [48]. We used 4 different quantitative measures for the synthetic validation as True Positives ($TP = \frac{N_B \cap N_R}{N_R}$), False Negatives ($FN = \frac{N_R - N_B \cap N_R}{N_R}$), False Positives ($FP = \frac{N_B - N_B \cap N_R}{N_R}$) and Overlap Measure ($OM = 2 \frac{N_B \cap N_R}{N_B + N_R}$) between the estimated vessel map and the ground truth vessel map. N_R is the number of reference ground truth voxels, and N_B is the number of voxels detected by our algorithm in synthetic data. On the generated 10 synthetic volumes, Table V tabulates average TP, FN, FP and OM rates with standard deviation. On average, TP and OM ratios were obtained $95.50 \pm 0.858\%$, $94.37 \pm 1.178\%$, FN $4.50 \pm 0.858\%$, and FP $6.65 \pm 1.865\%$. It also tabulates the number of ground truth bifurcations in each dataset and corresponding number of bifurcations detected with vessel tractography. As seen, most of the branches are detected by our automatic branch detection method. In average, 97.38% percentage of the branches, only missing the very short branches (≤ 4 -5 voxels length), with 1.54% standard deviation is detected.

We also tested the performance of vessel tractography by adding two levels of salt and pepper noise and Gaussian noise with two different variances to the synthetic volumes, and compared our results with the region growing (RG) algorithm. For simplicity, first three datasets, which are the sample datasets available on-line [54], are used in the noise experiments. Table VI shows the comparison of the region growing algorithm with our method (VesselTractography). Our algorithm is more resistive to salt and pepper noise compared to the region growing algorithm that uses a neighborhood intensity similarity criterion. Similarly, the performance of our method in the presence of two levels of Gaussian noise: $\sigma_{noise}^2 = 20$, $\sigma_{noise}^2 = 60$ is reported in Table VII.

TABLE IV
INTENSITY CRITERIA FOR VESSEL TRACTOGRAPHY: CT HU (HOUNSFIELD UNITS) ARE SCALED TO (0, 255).

Location	$\mu\Omega_0$	$\mu\Omega_1$	$\mu\Omega_2$	$\mu\Omega_3$
Proximal	135.17 ± 33.67	41.49 ± 16.72	55.65 ± 24.32	135.17 ± 33.67
	$\mu\Omega_1/\mu\Omega_0$	0.307 ± 0.063	$\mu\Omega_2/\mu\Omega_1$	0.412 ± 0.186
Distal	92.03 ± 28.21	41.49 ± 16.72	33.17 ± 19.32	92.03 ± 28.21
	$\mu\Omega_1/\mu\Omega_0$	0.455 ± 0.07	$\mu\Omega_2/\mu\Omega_1$	0.360 ± 0.142

TABLE V
SEGMENTATION AND BRANCH DETECTION RESULTS OF VESSEL TRACTOGRAPHY ON TEN SYNTHETIC VASCULAR IMAGES

	TP (%)	FN (%)	FP (%)	OM (%)	Number of bifurcations	Number of bifurcations detected
Data 1	94.30	5.7	8.45	93.03	99	97
Data 2	94.77	5.23	4.88	93.76	49	49
Data 3	96.13	3.87	4.76	95.70	199	195
Data 4	95.72	4.28	7.25	94.32	139	134
Data 5	96.02	3.98	4.50	95.77	159	155
Data 6	96.79	3.21	4.77	96.04	109	108
Data 7	94.42	5.58	8.87	92.89	79	79
Data 8	95.93	4.07	5.99	95.02	299	290
Data 9	94.79	5.21	7.99	93.49	259	253
Data 10	96.15	3.85	9.04	93.72	499	483
Avg.±std	95.50±0.858	4.50±0.858	6.65±1.865	94.37±1.178	Avg. OV±std	97.38±1.54

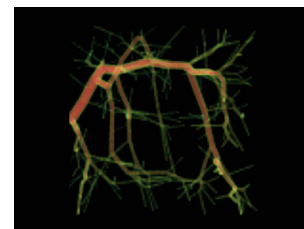
Figure 9 presents an example volume from the synthetic vascular dataset of Hamarneh and Jassi's work [48], and the results of our algorithm on the data #1 (volume size $101 \times 101 \times 101$ voxels) are depicted. Top frame shows a volume rendering of the 3D vascular data. The user selects a single seed, which is shown with a yellow sphere, over one of the branches marked in Fig. 9.(b). Then, the entire centerline tree (depicted by green in (b)) is extracted automatically by our method. The branch coordinates that are found during the execution of our algorithm are also shown in (b) by red spheres. Vessel tree with radial thickness superimposed as the envelope of spheres is shown in (c) (pink).

Figure 10 depicts the result of our algorithm on another dataset from [48] with additional salt and pepper noise of weight 0.2 (probability of noise). After selecting a single seed on one of the branches, the entire tree is captured automatically. Extracted centerline of the volume is shown in green, and the vessel tree with radial thickness is shown in orange on the right.

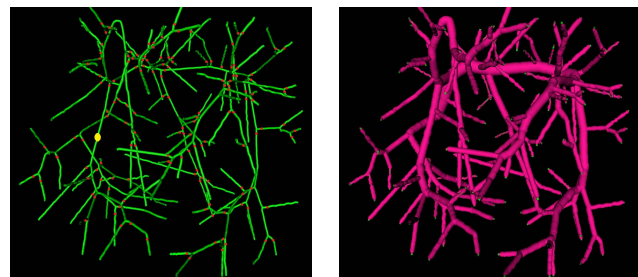
Our algorithm was able to capture the vessel structures and branches in all cases, as may be observed from both the quantitative and qualitative results with a slightly reduced performance as the level of noise is increased, which is expected.

B. Rotterdam Coronary Artery Evaluation

We have performed quantitative validation via testing on the database provided as part of the Rotterdam Coronary Artery Algorithm Evaluation Framework [51]. This framework facilitates standardized evaluations of centerline extraction methods



(a) Synthetic vascular dataset1: Volume rendering.



(b) Extracted centerline is indicated by green, detected branch coordinates by red, and seed point by yellow; (c) Extracted surface (pink) superimposed on centerline, which provides radius information of the vessel at each centerline point.

Fig. 9. Extracted vessel tree from the synthetic vascular dataset 1.

over the same datasets with ground truth and with standard performance measures. So far, the results of 22 methods are evaluated in this framework². The proposed segmentation framework was applied to all 32 datasets (including the 8 training and 24 testing data sets), and the results were submitted to the organizers for extracting the evaluation parameters.

²Please note that these results were obtained at the time of this writing (Oct 2012) and that the evaluation framework is continuously updated.

TABLE VI

COMPARISON OF THE SEGMENTATION RESULTS OF VESSELTRACTOGRAPHY WITH REGION GROWING (RG): ADDITIONAL SALT & PEPPER NOISE WITH WEIGHTS OF 0.05 AND 0.2.

	Measure (%)	data 1		data 2		data 3	
		RG	VesselTractography	RG	VesselTractography	RG	VesselTractography
Weight=0.05	TP	66.28	93.28	65.91	94.02	69.91	94.91
	FN	33.72	6.72	34.09	6.08	30.09	5.09
	FP	0.19	8.83	0.20	6.09	0.63	5.33
	OM	79.63	92.31	79.35	93.97	82.28	94.80
Weight=0.2	TP	63.02	92.04	48.92	93.21	60.10	93.54
	FN	36.98	7.96	51.08	6.79	39.90	6.46
	FP	1.22	8.91	0.60	6.13	0.17	5.82
	OM	76.74	91.60	65.44	92.35	74.99	92.49

TABLE VII

PERFORMANCE OF VESSEL TRACTOGRAPHY IN THE PRESENCE OF TWO LEVELS OF GAUSSIAN NOISE: $\sigma^2 = 20$, $\sigma^2 = 60$.

Measure (%)	data 1		data 2		data 3	
	$\sigma^2 = 20$	$\sigma^2 = 60$	$\sigma^2 = 20$	$\sigma^2 = 60$	$\sigma^2 = 20$	$\sigma^2 = 60$
TP	92.89	90.65	93.78	91.43	94.23	92.28
FN	7.11	9.35	6.22	8.57	5.77	7.72
FP	8.45	8.97	6.73	7.92	6.13	6.86
OM	92.27	90.82	93.54	91.73	94.06	92.76

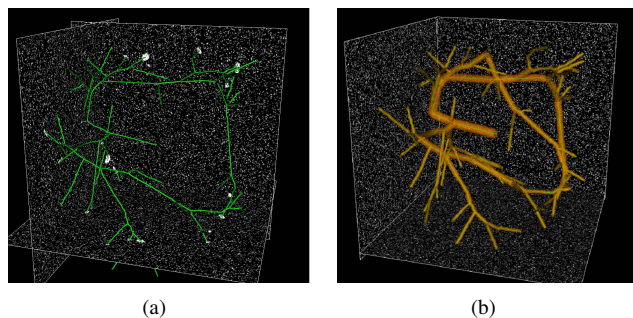


Fig. 10. Extracted vessel tree example from the synthetic vascular dataset with salt and pepper noise of weight 0.2. Left: Centerline; Right: Vessel surface constructed from the envelope of spheres.

Four arteries are provided for extraction from the coronary tree; to provide guidance on these arteries, the four reference points (Point A, B, S, E) are also provided for each data. The evaluation framework consists of three categories that describe the amount of user-interaction required: Automatic extraction methods, methods with minimum user interaction (semi-automatic) and interactive extraction methods. For the automatic extraction category, the methods find the centerlines of coronary arteries without user-interaction. In order to evaluate the performance of the automatic coronary artery centerline extraction methods, two points from the proximal (Point A) and distal (Point B) region per vessel are provided to extract the coronary artery of interest. These points are only used for guidance (to select the correct artery) and not for use in the automatic segmentation algorithms. In the second category, the users are allowed to use one point per vessel as input for the algorithm. This can be either one of the points: Point A, Point B, Point S (the start point of the centerline), Point E (the end point of the centerline), or Point U (any manually defined point). All methods that require more user-interaction than one point per vessel as input are part of the interactive extraction methods category. In this category, methods can use e.g. both points S and E from category 2, a series of manually clicked positions, or one point and a user-

defined threshold. We submitted our method to the second category; semi-automatic extraction, which provides one seed per vessel tree branch. As the user is allowed to use one seed per branch in this category, we selected 3-4 points per dataset to increase the accuracy of our results. The user is able to select a seed from any contrasted region along the vessel, hence, in this challenge, our method is categorized as a semi-automatic method with Point U interaction.

Accuracy and overlap scores for the segmented vessels are calculated as described in [50]. There are three overlap scores: *Overlap* (OV), *Overlap until first error* (OF) and *Overlap with > 1.5 mm vessel* (OT). These scores measure the overlap between the segmented centerlines and a ground truth centerline derived from manual segmentations by human experts. The accuracy scores evaluate the distance to the ground truth centerline. For instance, *Average distance inside vessel* (AI) measure describes the extraction accuracy if the centerline is located within the vessel. The scores are scaled so that 0 indicates complete failure, 50 corresponds to a result within the human inter-observer variability, and 100 is a perfect result. The average overlap and accuracy scores for our algorithm are presented in Table VIII. Nearly complete segmentation of the target vessels, with 96.4% OV, 69.9% OF, and 97.0% OT scores, are obtained. This leads to high overlap scores, with an average of 64.4 for the OV score, 70.3 for the OT score i.e., significantly better than the human inter-observer variability, and OF score is 51.6. The average distance inside the vessel to the ground truth centerline is 0.36 mm, and we obtained 30.7 for average AI score. Finally, the table shows statistics for the 'rank'. For each of the evaluated vessels, the 22 evaluated methods were ranked and assigned a number (1-22) representing its rank. If a method would always get the best results, it would get an average rank of 1.0. Comparison of our algorithm, with the 22 methods in the Rotterdam challenge are shown in Table IX. Our algorithm ranks first in the semi-automatic category, since on average, only one seed point (Point U) is used per vessel, whereas the other five non-automatic methods among the top 9 rank require more seeds (e.g. ≥ 2 such as at least Point S and Point E), while the four of them require no seeds (See "User interaction (per vessel)" column from Table IX). Our method ranks the 6th according to the overlap scores (See "Avg. Ov. rank"). For the overall results, it ranks the 10th (See "Avg. rank") among 22 methods. The first five methods are the interactive methods that use more than two seed points per vessel. Typically, the

seed points include the Point S and Point E. Although, in the Rotterdam challenge, the start and end points are provided for each dataset for a fair comparison, in real scenarios, it is hard to track particularly the end point of the vessel, therefore, our algorithm's lack of requirement for an end point is an advantage over those methods. The other four methods are the automatic methods that are mainly hybrid techniques, which include several pre and post processing steps such as heart extraction, Hessian-based enhancement and morphology, and do not provide the lumen thickness information. For further information about the methods, see [51]. To summarize, our algorithm has the following advantages over earlier methods: since the user may select a single seed from any contrasted region over the vessel, it is easy-to-use and requires almost no training when compared to the interactive methods that required the start and end points of an artery. Additionally, the proposed method simultaneously detects both the thickness of the vessel lumen as well as the centerline of the vessel structure, which may provide advantage for the further analysis of the lumen thickness profile.

Figure 11 shows sample visualizations of the results from training dataset 1, 2 and 6 of Rotterdam coronary artery database.

Our method is relatively fast, as it is a centerline-based method. The runtime of our algorithm with 3D visualization is ~ 9 minutes for a complete CTA vessel tree from a volume of typical size with $512 \times 512 \times 441$ voxels running on a PC with 2.67 GHz dual processor. We also added an option to our vessel tractography program for single branch extraction (without branch detection), which takes about a minute. Table IX provides also the runtime comparison with other methods.

TABLE IX
COMPARISON OF THE PROPOSED METHOD TO 22 EXISTING CORONARY CENTERLINE EXTRACTION METHODS IN ROTTERDAM CHALLENGE

Method	Avg. Ov. rank	Avg. Acc. rank	Avg. rank	Computation time (per dataset)	User interaction (per vessel)
Friman et al.	3.40	3.09	3.25	6 min.	2 - 5 pnts
Schaap et al.	4.76	2.48	3.62	22 min.	2.2
Wang and Smeedy	5.83	6.60	6.21	2 min.	3
Szymczak	7.67	5.24	6.45	30 min.	Point S, E
Lesage et al.	3.91	9.45	6.68	4 min.	Point S, E
Kitamura et al.	10.70	3.50	7.10	2 min. and 40 sec.	
Zambal et al.	11.25	6.70	8.97	4-8 min.	
Yang et al.	8.61	9.46	9.04	2 min.	None
COR Analyzer	12.27	5.96	9.12	4-6 min.	
VesselTractography	7.37	14.00	10.69	8 - 10 min.	Point U
Krissian et al.	7.50	15.24	11.37	7 hrs	Point E
Tek et al.	14.30	10.35	12.33	< 30 sec.	
Bauer and Bischof	9.96	14.80	12.38	10 min.	
Kitslaar et al.	15.41	9.74	12.58	70 sec.	
Metz et al.	9.61	15.95	12.78	12 min.	Point S and E
Wang et al.	12.00	17.23	14.61	45 minutes	Point S
Wang and Smedby	15.64	14.05	14.85	5 minutes	
Dikici et al.	12.77	17.07	14.92	5 minutes	Point E
Mohan et al.	12.28	18.14	15.21		3 to 5 points
Hernandez Hoyos et al.	16.12	15.24	15.68	2-6 minutes	thresh. + 1 point
Zhang et al.	13.86	18.84	16.35	3-6 minutes	3 to 10 points
Castro et al.	18.17	19.76	18.97	30 minutes	Point S

C. Qualitative Visual Scores on Clinical Cases

Next, we applied our method to the extraction of the coronary arteries over CTA volumes from our clinical partner site. We collected 10 cardiac CTA datasets from Cardiology Department of Yeditepe University Hospital, which are acquired using a Philips Brilliance 64 slice CTA machine.

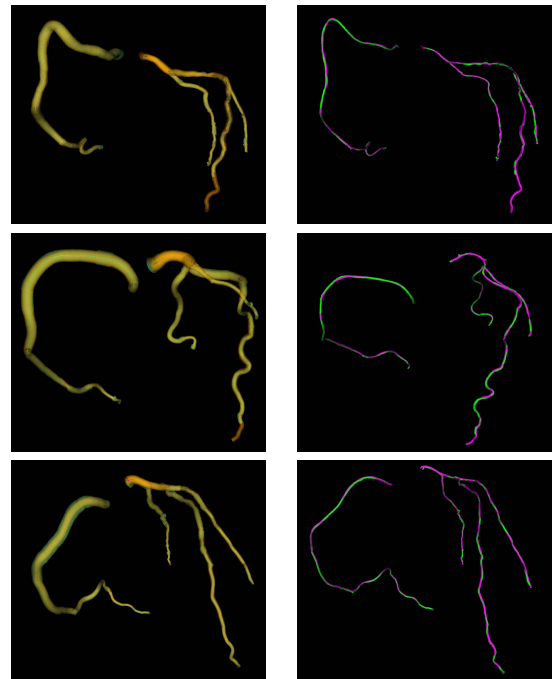


Fig. 11. Top to Bottom: Visualization of the results from experiments for quantitative validation using the Rotterdam cardiac data set # 1, 2 and 6. Left Column: Results with radius information for the ground truths (orange) and corresponding vessel trees (pale green) ; Right Column: Centerline of the ground truths (purple) and corresponding vessel trees (green).

For a qualitative evaluation; in each dataset, the cardiologist expert in the team evaluated the results of the extracted artery tree ($\geq 1.0mm$ vessel lumen thickness), which are segmented by selecting a single seed. Our method detected all branches with $\geq 1.0mm$ vessel lumen thickness. Then, the expert specifically gave scores (0-5) to RCA (Right Coronary Artery), LM (Left Main), LAD (Left Anterior Descending) and LCX (Left Circumflex Artery) by considering (i) length (the length of the vessel from ostium to the end ($\geq 0.5mm$)); (ii) thickness (vessel lumen thickness); (iii) centerline (central lumen line) of each artery, where 0 means complete failure, and 5 is the complete success. The expert was instructed to give a 5 score if the all the above three criteria visually looked complete (perfect); drop 0.5 points if any one of the three criteria were not “perfect”, but “acceptable”; drop 0.5 points if two of the criteria were not “perfect” but “acceptable”. If all the three criteria are “acceptable”, then the score would be 3.5. (lower rankings would continue in this manner with “low performing”, and “complete failure”).

The scores (“perfect”, “acceptable”, “low performing”) for the three criteria are specified as follows: For the length criterion; perfect score indicates the vessel is extracted from ostium to leaf (ostium to $0.5mm$ lumen thickness), acceptable score means the clinically relevant part of the vessel (ostium to $1.5mm$) is extracted correctly, and low performing score corresponds to the extraction of vessel from ostium to $> 1.5mm$. In order to evaluate the results of the lumen thickness and centerline, 20 sample points that include all specific cases are selected along each branch. For the vessel thickness criterion; perfect score indicates the estimated lumen thickness $\geq 90\%$

TABLE VIII
SUMMARY OF ROTTERDAM TEST RESULTS

Measure	% / mm			score			rank		
	min.	max.	avg.	min.	max.	avg.	min.	max.	avg.
OV	75.5%	100.0%	96.4%	38.8	100.0	64.3	1	14	6.85
OF	6.2%	100.0%	69.9%	3.1	100.0	51.6	1	19	7.80
OT	75.5%	100.0%	97.0%	38.8	100.0	70.3	1	16	5.89
AI	0.23 mm	0.58 mm	0.36 mm	17.9	59.3	30.7	3	19	12.82
Total							1	19	9.84

fits to the vessel lumen, acceptable score determines the fit between 80% and 90%, and low performing score signifies $< 80\%$ fit to the vessel lumen. For the centerline criterion; perfect score represents propagation of the estimated centerline $\leq 0.5mm$ away from the central lumen, acceptable score means the estimated centerline propagates between $0.5mm$ and $1mm$ away from the central lumen, and low performing score indicates the estimated centerline propagates $\geq 1.5mm$ away from the central lumen. Scores ≥ 4 were obtained in each criterion for each coronary branch. The visual scores for the average of the three criteria are tabulated in Table X.

D. Quantitative Validation of Branch Detection on Clinical Cases

In addition, we evaluated the proposed branch detection algorithm on the same 10 patient CTA dataset of Section III-C. First, we asked the cardiologist expert to mark the origins of the clinically relevant branches ($> 0.5mm$), i.e. the bifurcation points, in each CTA volume blindly (that is without seeing our segmentation and detection results). This effort resulted in total 147 bifurcation annotations, whose physical coordinates were recorded³. Then, the branching points were detected by our algorithm, and it was observed that, on average, the 92.66% of the marked points can be detected successfully in a $< 1.5mm$ elliptical region ($< 1.5mm$ is the longer axis, which is along the centerline of the vessel. The length becomes $< 0.85mm$ in the orthogonal directions of the vessel). In Table XI, the number of bifurcation points marked by the expert, the number of detected branching points in the elliptical region defined, and the overlap score (OM = % # detected / # marked) are shown for each dataset. The missing branches are observed to have the $< 1.0mm$ thickness.

Sample extracted arteries for CTA datasets of patient 1, 2, 5, 6, 8 and 9 are depicted in Figure 12.

TABLE X
VISUAL SCORES OF VESSEL TRACTOGRAPHY ON 10 CTA VOLUMES FROM PATIENT 1 (PT 1) TO PATIENT 10 (PT 10)

	Pt 1	Pt 2	Pt 3	Pt 4	Pt 5	Pt 6	Pt 7	Pt 8	Pt 9	Pt 10
RCA	5	5	5	5	5	5	5	4	5	5
LM	5	5	5	5	5	5	5	5	4.5	5
LAD	5	5	5	5	4.5	4.5	5	4	4.5	5
LCX	4	5	5	5	5	4.5	5	4	5	5

IV. DISCUSSION AND CONCLUSION

In this paper, we presented a vessel tractography idea for extraction of coronary arteries from CTA scans. For this purpose,

³The bifurcation annotations along with the given dataset can be reached from: <http://vpa.sabanciuniv.edu/sites/cabdvd/>

we designed a fast and novel tubular structure segmentation method, which constructs an intensity-based tensor that traces a vessel, and used it in a tractography framework, inspired from the DTI field. In our model, we created planar rank 2 tensors along the centerline, where the eigenvector that corresponds to the smallest eigenvalue represents the vessel orientation. Intuitively, planar tensors are a generalization of placing a collection of disks each lying in the plane perpendicular to the center line of the vessel. The inverse of this planar tensor, which will be an elongated anisotropic ellipsoid, can be also used as an alternative to our planar tensor model. In this case, the principal eigenvector represents the vessels orientation, and the smallest two eigen values (λ_2 and λ_3) can be used as a measure for the vessel extraction. The vessel tractography algorithm is initialized with a single seed, located on the centerline, then, an entire vessel tree is automatically segmented by incorporating our automatic branch detection method. During the extraction of the centerline, the vessel lumen surface is estimated without further passes on the algorithm. The performance of our method was evaluated on synthetic complex-structured, varying-contrast datasets, where we obtained around 95% overlap ratios. Within the Rotterdam Coronary Artery Algorithm Evaluation Framework, the proposed method is the 10th among all 22 methods, and is the 1st among the semi-automatic algorithms. In a qualitative expert evaluation, we tested our algorithm on clinical datasets, where high visual scores were obtained. Moreover, we performed a quantitative validation of the proposed branch detection method on the same clinical CTA datasets, which were manually annotated for bifurcations by an expert.

Limitations of our method include requirement of user-interactivity. Even though the method needs only a single seed point for the extraction of a vessel tree, our method can become full-automatic by applying a heart extraction method and ostium localization in the preprocessing. Furthermore, looking at the tubular segmentation problem from a tensor estimation and tractography point of view, several new directions for improvement of our work emerge following the presented work: (1) Intensity measurements other than the piece-wise constant model can be utilized. For instance, a Gaussian intensity density model with mean and variances of inside and outside vessel, or non-parametric density estimators can be utilized to represent possible vessel intensity distributions; (2) In order to have a smoother centerline, simple streamline tractography can be extended to a geodesic tractography approach using the vessel tensor as the metric; (3) Rather than a single tensor model, a mixture of tensors [55] could be utilized to naturally handle the branching scenarios; (4) New vessel models, i.e instead of a cylinder, e.g a cone or a half ellipsoid, can be proposed; (5) In order to handle the branch detection problem

TABLE XI
OVERLAP SCORES OF BRANCH DETECTION ON 10 CTA VOLUMES FROM PATIENT 1 (PT 1) TO PATIENT 10 (PT 10)

	Pt 1	Pt 2	Pt 3	Pt 4	Pt 5	Pt 6	Pt 7	Pt 8	Pt 9	Pt 10
# marked bifurcations	13	15	23	15	17	12	11	11	12	18
# detected bifurcations	12	13	22	13	15	11	10	11	12	17
OM(%)	92.31	86.67	95.65	86.67	88.24	91.67	90.91	100	100	94.44

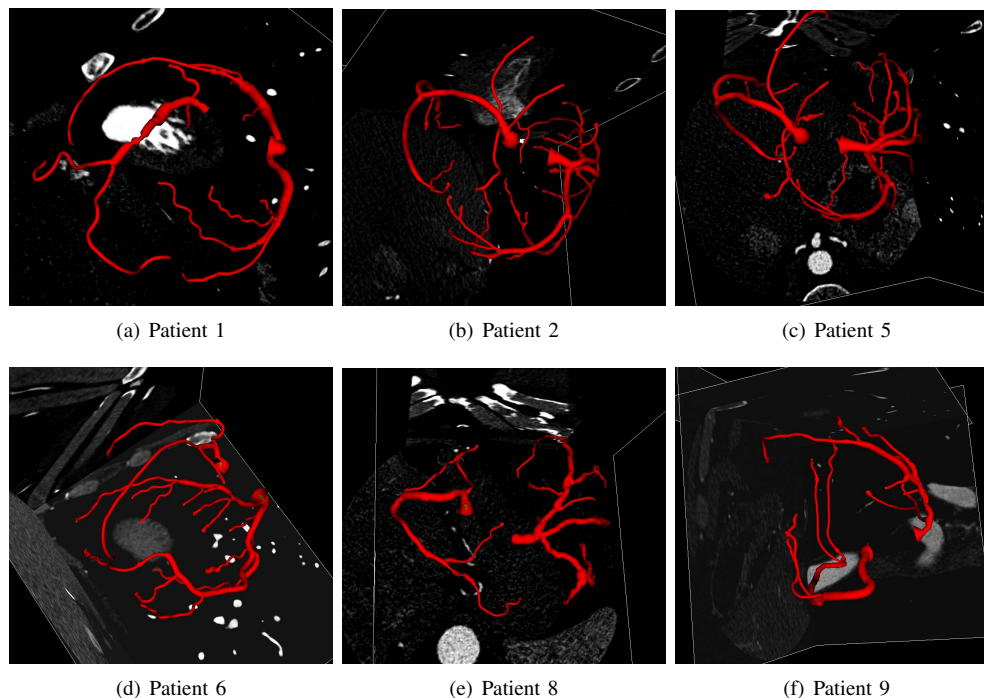


Fig. 12. Visualization of the extracted arteries from CTA volumes of patient # 1, 2, 5, 6, 8, and 9.

in the tensor model itself, we are extending our work to higher dimensional tensors and orientation distribution functions. Our ongoing work involves pursue of these interesting research directions.

ACKNOWLEDGMENT

This work was supported by Turkish Scientific and Technical Research Council(TUBITAK)-BMBF Germany Intense Cooperation Grant (Tubitak Grant No:108E162): "Assessment of Fluid Tissue Interaction Using Multi-Modal Image Fusion for Characterization and Progression of Coronary Atherosclerosis".

REFERENCES

- [1] C. Kirbas and F. Quek, "A review of vessel extraction techniques and algorithms," *ACM Comput. Surv.*, vol. 36, pp. 81–121, June 2004.
- [2] P. Felkel, R. Wegenkittl, and A. Kanitsar, "Vessel Tracking in Peripheral CTA Datasets - An Overview," in *IEEE Spring Conference on Computer Graphics (SCCG 2001)*, 2001, pp. 232–239.
- [3] J. S. Suri, K. C. Liu, L. Reden, and S. Laxminarayan, "A review on MR vascular image processing algorithms: Acquisition and prefiltering: part I," *IEEE T. Inf. Technol. Biomed.*, vol. 6, no. 4, pp. 324–337, Dec. 2002.
- [4] J. S. Suri, K. Liu, L. Reden, and S. Laxminarayan, "A review on mr vascular image processing: skeleton versus nonskeleton approaches: part ii," *IEEE Transactions on Information Technology in Biomedicine*, vol. 6, no. 4, pp. 338–350, 2002.
- [5] K. Bhler, P. Felkel, and A. L. Cruz, "Geometric methods for vessel visualization and quantification – a survey," in *In Geometric Modelling For Scientific Visualization*. Springer-Verlag, 2002, pp. 399–420.
- [6] D. Lesage, E. D. Angelini, I. Bloch, and G. Funka-Lea, "A review of 3D vessel lumen segmentation techniques," *Med. Imag. Anal.*, vol. 13, no. 6, pp. 819–845, Dec. 2009.
- [7] D. P. Zhang, "Coronary artery segmentation and motion modelling," *PhD Thesis, Imperial College London*, 2010.
- [8] T. Koller, G. Gerig, G. Szekely, and D. Dettwiler, "Multiscale detection of curvilinear structures in 2-d and 3-d image data," in *Computer Vision, 1995. Proceedings., Fifth International Conference on*, jun 1995, pp. 864–869.
- [9] C. Lorenz, I. Carlsen, T. Buzug, C. Fassnacht, and J. Weese, "Multi-scale line segmentation with automatic estimation of width, contrast and tangential direction in 2D and 3D medical images," in *CVRMed-MRCAS'97*, ser. Lecture Notes in Computer Science, J. Troccaz, E. Grimson, and R. Mösger, Eds. Berlin/Heidelberg: Springer Berlin / Heidelberg, 1997, vol. 1205, ch. 24, pp. 233–242.
- [10] Y. Sato, S. Nakajima, H. Atsumi, T. Koller, G. Gerig, S. Yoshida, and R. Kikinis, "3D Multi-scale line filter for segmentation and visualization of curvilinear structures in medical images," in *CVRMed-MRCAS '97: Proceedings of the First Joint Conference on Computer Vision, Virtual Reality and Robotics in Medicine and Medial Robotics and Computer-Assisted Surgery*. London, UK: Springer-Verlag, 1997, pp. 213–222.
- [11] A. F. Frangi, W. J. Niessen, K. L. Vincken, and M. A. Viergever, "Multiscale Vessel Enhancement Filtering," *Medical Image Computing and Computer-Assisted Intervention MICCAI'98*, pp. 130–137, 1998.
- [12] S. D. Olabbariaga, W. J. Niessen, and M. Breeuwer, "Evaluation of hessian-based filters to enhance the axis of coronary arteries in ct images," in *Computer Assisted Radiology and Surgery*, 2003, pp. 1191–1196.
- [13] P. Orłowski and M. Orkisz, "Efficient computation of Hessian-based

- enhancement filters for tubular structures in 3D images," *IRBM*, vol. 30, no. 3, pp. 128–132, Jun. 2009.
- [14] K. Krissian, "Flux-based anisotropic diffusion applied to enhancement of 3-d angiograms," *IEEE Trans. Med. Imaging*, vol. 21, no. 11, pp. 1440–1442, 2002.
- [15] R. Manniesing, M. Viergever, and W. Niessen, "Vessel enhancing diffusionA scale space representation of vessel structures," *Medical Image Analysis*, vol. 10, no. 6, pp. 815–825, Dec. 2006.
- [16] L. Risser, F. Plouraboue, and X. Descombes, "Gap Filling of 3-D Microvascular Networks by Tensor Voting," *Medical Imaging, IEEE Transactions on*, vol. 27, no. 5, pp. 674–687, 2008.
- [17] M. W. Law and A. C. Chung, "Three dimensional curvilinear structure detection using optimally oriented flux," in *Proceedings of the 10th European Conference on Computer Vision: Part IV*. Berlin, Heidelberg: Springer-Verlag, 2008, pp. 368–382.
- [18] D. Lesage, E. D. Angelini, I. Bloch, and G. Funka-Lea, "Design and study of flux-based features for 3d vascular tracking," in *Proceedings of the Sixth IEEE international conference on Symposium on Biomedical Imaging: From Nano to Macro*, ser. ISBI'09. Piscataway, NJ, USA: IEEE Press, 2009, pp. 286–289.
- [19] R. Rodríguez, T. E. Alarcón, and O. Pacheco, "A new strategy to obtain robust markers for blood vessels segmentation by using the watersheds method," *Comput. Biol. Med.*, vol. 35, pp. 665–686, October 2005.
- [20] N. Passat, C. Ronse, J. Baruthio, J. P. Armspach, and J. Foucher, "Water-shed and multimodal data for brain vessel segmentation: Application to the superior sagittal sinus," *Image Vision Comput.*, vol. 25, pp. 512–521, April 2007.
- [21] N. Passat, C. Ronse, J. Baruthio, J. P. Armspach, and C. Maillot, "Magnetic resonance angiography: From anatomical knowledge modeling to vessel segmentation," *Medical Image Analysis*, vol. 10, no. 2, pp. 259–274, Apr. 2006.
- [22] B. Bouraoui, C. Ronse, J. Baruthio, N. Passat, and P. Germain, "3D segmentation of coronary arteries based on advanced Mathematical Morphology techniques," *Computerized Medical Imaging and Graphics*, vol. 34, no. 5, pp. 377–387, July 2010.
- [23] M. H. F. Wilkinson and M. A. Westenberg, "Shape preserving filament enhancement filtering," in *Proceedings of the 4th International Conference on Medical Image Computing and Computer-Assisted Intervention*, ser. MICCAI '01. London, UK, UK: Springer-Verlag, 2001, pp. 770–777.
- [24] B. Caldaïrou, B. Naegel, and N. Passat, "Segmentation of complex images based on component-trees: Methodological tools," in *Proceedings of the 9th International Symposium on Mathematical Morphology and Its Application to Signal and Image Processing*, ser. ISMM '09. Berlin, Heidelberg: Springer-Verlag, 2009, pp. 171–180.
- [25] L. M. Lorigo, O. D. Faugeras, W. E. Grimson, R. Keriven, R. Kikinis, A. Nabavi, and C. F. Westin, "CURVES: curve evolution for vessel segmentation," *Med Image Anal*, vol. 5, no. 3, pp. 195–206, 2001.
- [26] R. Manniesing, M. Viergever, and W. Niessen, "Vessel axis tracking using topology constrained surface evolution," *Medical Imaging, IEEE Transactions on*, vol. 26, no. 3, pp. 309–316, march 2007.
- [27] X. Zhu, Z. Xue, X. Gao, Y. Zhu, and S. Wong, "Voles: Vascularity-oriented level set algorithm for pulmonary vessel segmentation in image guided intervention therapy," in *Biomedical Imaging: From Nano to Macro, 2009. ISBI '09. IEEE International Symposium on*, 28 2009-july 1 2009, pp. 1247–1250.
- [28] S. Worz and K. Rohr, "Segmentation and quantification of human vessels using a 3-d cylindrical intensity model," *Image Processing, IEEE Transactions on*, vol. 16, no. 8, pp. 1994–2004, aug. 2007.
- [29] O. Friman, M. Hindennach, C. Kühnel, and H.-O. Peitgen, "Multiple hypothesis template tracking of small 3D vessel structures," *Med. Imag. Anal.*, vol. 14, no. 2, pp. 160–171, Apr. 2010.
- [30] D. Nain, A. J. Yezzi, and G. Turk, "Vessel segmentation using a shape driven flow," in *MICCAI (1)*, 2004, pp. 51–59.
- [31] K. Krissian, G. Malandain, N. Ayache, R. Vaillant, Y. Troussset, I. S. Antipolis, and S. A. C. (france), "Model based detection of tubular structures in 3d images," 2000.
- [32] M. Gulsun and H. Tek, "Robust vessel tree modeling," in *Medical Image Computing and Computer-Assisted Intervention MICCAI 2008*, ser. Lecture Notes in Computer Science, D. Metaxas, L. Axel, G. Fichtinger, and G. Székely, Eds. Springer Berlin / Heidelberg, 2008, vol. 5241, pp. 602–611.
- [33] H. Li and A. J. Yezzi, "Vessels as 4-d curves: Global minimal 4-d paths to extract 3-d tubular surfaces and centerlines," *IEEE Trans. Med. Imaging*, vol. 26, no. 9, pp. 1213–1223, 2007.
- [34] V. Mohan, G. Sundaramoorthi, and A. Tannenbaum, "Tubular surface segmentation for extracting anatomical structures from medical imagery," *IEEE Trans. Med. Imag.*, pp. 1945–1958, 2010.
- [35] F. Benmansour and L. D. Cohen, "Tubular structure segmentation based on minimal path method and anisotropic enhancement," *Int. J. Comput. Vision*, vol. 92, pp. 192–210, April 2011.
- [36] D. Lesage, E. D. Angelini, I. Bloch, and G. Funka-Lea, "Bayesian maximal paths for coronary artery segmentation from 3d ct angiograms," pp. 222–229, 2009.
- [37] S. Zambal, J. Hladuvka, A. Kanitsar, and K. Buhler, "Shape and appearance models for automatic coronary artery tracking," in *MICCAI 2008 Contest: 3D Segmentation in Clinic: A Grand Challenge*, 2008.
- [38] C. Bauer and H. Bischof, "Extracting curve skeletons from gray value images for virtual endoscopy," in *Proceedings of the 4th international workshop on Medical Imaging and Augmented Reality*, ser. MIAR '08. Berlin, Heidelberg: Springer-Verlag, 2008, pp. 393–402.
- [39] L. Antiga and D. Steinman, "Robust and objective decomposition and mapping of bifurcating vessels," *Medical Imaging, IEEE Transactions on*, vol. 23, no. 6, pp. 704–713, june 2004.
- [40] J. Zhou, S. Chang, D. N. Metaxas, and L. Axel, "Vascular structure segmentation and bifurcation detection," in *ISBI*, 2007, pp. 872–875.
- [41] H. Li, A. Yezzi, and L. Cohen, "3d multi-branch tubular surface and centerline extraction with 4d iterative key points," in *Proceedings of the 12th International Conference on Medical Image Computing and Computer-Assisted Intervention: Part II*, ser. MICCAI '09. Berlin, Heidelberg: Springer-Verlag, 2009, pp. 1042–1050.
- [42] S. Cetin, G. Unal, A. Demir, A. Yezzi, and M. Degertekin, "Vessel tractography using an intensity based tensor model," *The MICCAI Workshop on Computing and Visualization for (Intra)Vascular Imaging (CVI)*, 2011.
- [43] S. Halliburton, A. Stillman, and R. White, "Noninvasive quantification of coronary artery calcification: methods and prognostic value." *Cleve Clin J Med.*, 2002.
- [44] P. J. Basser, J. Mattiello, and D. LeBihan, "Estimation of the effective self-diffusion tensor from the nmr spin echo." *J Magn Reson B*, vol. 103, no. 3, pp. 247–254, Mar. 1994.
- [45] D. Kalman, "A Singularly Valuable Decomposition: The SVD of a Matrix," *The College Mathematics Journal*, vol. 27, no. 1, pp. 2–23, 1996.
- [46] K. Krissian and G. Malandain, "Synthetical test images for vascular segmentation algorithms," <http://lmi.bwh.harvard.edu/research/vascular/SyntheticVessels/SyntheticVesselImages.html>.
- [47] P. J. Basser, S. Pajevic, C. Pierpaoli, and A. Aldroubi, "Fiber tract following in the human brain using dt-mri data," *Magn. Reson. Med*, 2002.
- [48] G. Hamarneh and P. Jassi, "Vascusynth: Simulating vascular trees for generating volumetric image data with ground-truth segmentation and tree analysis," *Computerized Medical Imaging and Graphics*, vol. 34, no. 8, pp. 605–616, 2010.
- [49] C. Metz, M. Schaap, T. van Walsum, A. van der Giessen, A. Weustink, N. Mollet, G. P. Krestin, and W. Niessen, "Editorial: 3d segmentation in the clinic: A grand challenge ii - coronary artery tracking, miccai 2008 workshop proceedings," 2008.
- [50] M. Schaap, C. T. Metz, T. van Walsum, A. G. van der Giessen, A. C. Weustink, N. R. Mollet, C. Bauer, H. Bogunovice, C. Castro, X. Deng, E. Dikici, T. O'Donnell, M. Frenay, O. Friman, M. H. Hoyos, P. H. Kitslaar, K. Krissian, C. Khnel, M. A. Luengo-Oroz, and M. Orkisz, "Standardized evaluation methodology and reference database for evaluating coronary artery centerline extraction algorithms," *Medical Image Analysis*, vol. 13, pp. 701–714, 2009.
- [51] M. Schaap, C. Metz, T. V. Walsum, and W. Niessen, "Rotterdam coronary artery algorithm evaluation framework," <http://coronary.bigr.nl/centerlines/>.
- [52] Nokia, "Qt," <http://qt.nokia.com>.
- [53] W. Schroeder, K. Martin, and B. Lorensen, "The visualization toolkit, third edition. kitware inc," <http://www.vtk.org>.
- [54] H. Ghassan and J. Preet, "Vascusynth sample datasets," <http://vascusynth.cs.sfu.ca/Data.html>.
- [55] D. S. Tuch, "Q-ball imaging," *Magnetic Resonance in Medicine*, vol. 52, no. 6, pp. 1358–1372, Dec. 2004.